Research Article | Vol. 26, No. 24 | 26 Nov 2018 | OPTICS EXPRESS 31861
Optics EXPRESS

Modeling of second harmonic generation in hole-doped silicon-germanium quantum wells for mid-infrared sensing

JACOPO FRIGERIO,[1] ANDREA BALLABIO,[1] MICHELE ORTOLANI,[2,*] AND MICHELE VIRGILIO[3]

[1]*L-NESS, Dipartimento di Fisica, Politecnico di Milano, Polo Territoriale di Como, Via Anzani 42, I-22100, Como, Italy*
[2]*Dipartimento di Fisica, Sapienza Università di Roma, Piazzale Aldo Moro 5, I-00185 Rome, Italy*
[3]*Dipartimento di Fisica "E. Fermi", Università di Pisa, Largo Pontecorvo 3, I-56127 Pisa, Italy*
[*]*michele.ortolani@roma1.infn.it*

Abstract: The development of Ge and SiGe chemical vapor deposition techniques on silicon wafers has enabled the integration of multi-quantum well structures in silicon photonics chips for nonlinear optics with potential applications to integrated nonlinear optics, however research has focused up to now on undoped quantum wells and interband optical excitations. In this work, we present model calculations for the giant nonlinear coefficients provided by intersubband transitions in hole-doped Ge/SiGe and Si/SiGe multi-quantum wells. We employ a valence band-structure model for $Si_{1-x}Ge_x$ to calculate the confined hole states of asymmetric-coupled quantum wells for second-harmonic generation in the mid-infrared. We calculate the nonlinear emission spectra from the second-order susceptibility tensor, including the particular vertical emission spectra of valence-band quantum wells. Two possible nonlinear mid-infrared sensor architectures, one based on waveguides and another based on metasurfaces, are described as perspective application.

1. Introduction

Mid-infrared (MIR) photonics is receiving considerable attention due to the variety of envisaged applications in medical diagnostics [1], biochemistry studies [2,3], chemical analytics [4], and environmental monitoring for safety and security [5]. The interest towards the MIR resides in the presence of unique vibrational fingerprints of molecules in the wavelength range $\lambda = 5$ to 15 μm (photon energies from 80 to 240 meV). An important feature of molecular sensing techniques in the MIR is the direct probing of quasi-Lorentzian lineshapes of molecule absorption [6], as opposed to refractive index sensing, typically performed at a single wavelength in the visible (VIS) or near-infrared (NIR) by detection of angular shifts, as in surface plasmon resonance (SPR) sensors [7], or of phase shifts, as in Mach-Zhender interferometers, either fiber-based [1] or integrated in photonic chips [5]. In general, probing the molecular absorption lineshape (frequency, width, intensity and possible asymmetry) leads to better molecular specificity and higher information quality than refractive index sensing [3]. Measuring MIR spectral lineshapes is relatively straightforward in the gas phase [8] or liquid phase [4], however it is still a challenge for thin solid films deposited on a sensor surface [9]. Surface-enhanced transmission/reflection spectroscopy in the MIR of ultrathin molecular films with Fourier Transform interferometers has developed significantly in the last decade basing on plasmonic nanoantenna arrays [2,10,11], metasurfaces [7,3] and evanescent wave sensors [12,13], but major issues on molecular lineshape modification by near-field interactions and their conversion to detectable far-field signals have not been solved yet [9].

An entirely different path could be followed by introducing nonlinear emission spectroscopy in the MIR: with the radiation source positioned exactly at the molecule

#340238 https://doi.org/10.1364/OE.26.031861
Journal © 2018 Received 20 Jul 2018; revised 10 Sep 2018; accepted 6 Oct 2018; published 19 Nov 2018

Optics EXPRESS

location, the complex electromagnetic problem of multiple near-field/far-field conversions [14] could be greatly simplified [15]. MIR tunable laser pump beams are now available for use in future nonlinear photonic sensors in the MIR. Nonlinear frequency conversion in MIR optical parametric oscillators is progressing steadily [16]. Quantum cascade lasers provide an electrically pumped, continuous-wave platform for high-harmonic generation in the MIR [17–19]. However, nonlinear optics in the MIR presents technological challenges related to optical material transparency [20] and rescaling of VIS-NIR photonic architectures at longer wavelengths, therefore the exploration of unconventional approaches to nonlinear optics is much needed.

Besides classical approaches based on intrinsic nonlinearity of bulk crystals [21] and novel approaches based e.g. on nonlinear plasmonics [22] and phononics [23], an approach unique to the MIR is the exploitation of the giant nonlinearity of intersubband transitions (ISBTs) in doped multi quantum wells (MQW). This phenomenon is based on the giant dipole moment of a two-dimensional (2D) electron gas in a doped quantum well. In the simplest condition of one single parabolic band and quantum confinement along the MQW crystal growth direction *z*, the ground state is a 2D parabolic subband minimum occupied by the electron gas with density N_{2D}, and the excited states are 2D parabolic subbands at equal energy difference for all electronic states. Therefore, N_{2D} multiplies both the linear dipole moment at a given inter-subband transition (ISBT) energy and the second-order nonlinear tensor $\chi_{ijk}^{(2)}$ (where the indexes *i*,*j*,*k* run across the two equivalent in-plane directions *x*, *y* and the quantum confinement direction *z*). With typical values of N_{2D} in the range of 10^{11} cm^{-2}, the individual nonlinear coefficients, i.e. the elements of the tensor $\chi_{ijk}^{(2)}$, can reach values of the order of 10^5 pm/V [17,18,24–27], three to four orders of magnitude higher than those observed in the best nonlinear crystals. Similar behavior could be expected in principle for a 2D hole gas in the valence band, however the valence band structure is considerably more complex than the conduction band, as the former features heavy hole (HH), light hole (LH) and split off (SO) bands, while the latter features only one parabolic free electron band. The intervalence-band mixing at nonzero wavevector $\boldsymbol{k}$ results in strong nonparabolic dispersion of the hole states. In turn, the ISBT energy becomes a function of $\boldsymbol{k}$, making the ISBT spectrum more complex than that of a three-level system typically observed in electron-doped MQWs. Nevertheless, a giant $\chi_{ijk}^{(2)}$ can be designed for hole-doped MQWs by implementing accurate models of the valence band beyond the simple parabolic approximation, as we do here. Due to the peculiar selection rules of ISBTs involving both HH and LH states, the use of valence-band quantum wells opens up the exciting perspective of surface emission of SHG radiation by leveraging on the off-diagonal terms of the nonlinear susceptibility tensor $\chi_{xzx}^{(2)}$ [8,24,25].

The giant nonlinearity of ISBTs in MQWs was investigated more than two decades ago, both theoretically [24] and experimentally [25,26]. It has been recently revisited using metasurfaces [27] and plasmonic nanoresonators [17,18] providing strong field enhancement, which is extremely useful to enhance nonlinear effects and in turn allows for ultrathin nonlinear elements as opposed to relatively long interaction regions in integrated waveguides. Recent studies of nonlinearity in doped MQWs have focused on electron-doped InGaAs/AlInAs heterostructures ($In_{1-x}Ga_xAs$ wells and $Al_{1-x}In_xAs$ barriers) on InP substrates [17–19,27]. This material system represents an ideal platform for nonlinear MIR photonics because it can be approximated with the ideal single-parabolic band model; it features a band offset of 0.5 eV, quite higher than MIR photon energies of interest for molecular sensing; it has a high refractive index of 3.6 useful for strong mode-confinement in waveguides; and it can operate as active gain material to compensate for pump depletion and free-carrier losses [19]. However, compound semiconductor heterostructures are not suited for the mass-production of disposable sensing chips, which could instead be possible with silicon-foundry compatible group-IV semiconductor heterostructures such as SiGe/Si ($Si_{1-x}Ge_x$ wells and Si

Optics EXPRESS

barriers) and Ge/SiGe (Ge wells and $Si_{1-x}Ge_x$ barriers). The indirect-bandgap disadvantage of group-IV semiconductors does not play a role in unipolar MQW systems. Silicon photonic chips now include MQW structures for quantum-confined Stark effect modulators [28], quantum well IR photoionization (QWIP) detectors [29], integrated SiGe waveguides [30], and all-semiconductor plasmonic nanoresonators [10]. At the same time, the nonlinearity of ISBTs in doped Ge/SiGe and SiGe/Si MQWs is expected to be as large as that of their compound semiconductor counterparts, but it has not been calculated nor measured so far. In this work, we present an application study for MIR emission sensors based on second-harmonic generation (SHG) in hole-doped MQWs made of Ge/SiGe and SiGe/Si whose band offset of 0.5 eV enables MIR applications, unlike Ge/SiGe electron-doped MQWs that have an offset around 0.1 eV [31]. The paper is organized as follows: in Section 2 the silicon-germanium heterostructure material platform is introduced and three specific heterostructure designs are described; in Section 3, a model for the giant nonlinearity of ISBTs in the valence band of group-IV heterostructures is presented and SHG spectra are calculated; in Section 4, the feasibility of epitaxial material growth is discussed; in Section 5, two nonlinear MIR sensor architectures based on waveguide chips and plasmonic metasurfaces are proposed.

2. Material properties and model

MQWs in the valence band of Ge/Si systems can provide band offsets up to 0.5 eV for the heavy hole band, comparable to those of InGaAs/AlInAs systems, a high refractive index up to 4.0 for mode confinement and an extremely wide MIR transparency range especially in Ge-rich MQWs. The band offsets obtainable for the light hole band are generally smaller, depending on the composition and on the strain of the particular structure. The possibility for loss compensation by electrical or optical pumping cannot be excluded in the future, as optical gain has been predicted in Si/SiGe heterostructures [31]. The numerical modeling capability and the knowledge of the material parameters for group-IV heterostructures [32,33] has increased enormously in the last years. On these bases, we have constructed an accurate model for the valence band of $Si_{1-x}Ge_x$ heterostructures independently accounting for both strain and composition at any x between 0 and 1. This model has been used to design three heterostructures based on asymmetric coupled quantum wells (ACQWs) [14,17] suitable for SHG because the asymmetry of the structure breaks the inversion symmetry of the $Si_{1-x}Ge_x$ crystal. In particular we propose a Ge-rich heterostructure (Ge/SiGe design) and a Si-rich heterostructure (Si/SiGe design) that both exploit only HH to HH transitions for SHG; and another Ge-rich heterostructure (GeLH) where HH to LH ISBTs are exploited instead for SHG, enabling significant off-diagonal $\chi^{(2)}_{xzx}$ terms [24]. A scheme of the three designs is shown in Fig. 1: the well with higher Ge content x is labeled as “main well (M)” and the other well is labeled “secondary well (S)”. In all designs, the compressive strain of the well layer guarantees that the HH state of the main well is the ground state of the system which we label as HH0M. In this work, the series of excited HH states of the main well is labeled HH1M, HH2M etc. while the series of states for the secondary well is labeled HH0S, HH1S etc., and the LH and SO states of both wells are labeled accordingly. This nomenclature is justified by the weak hybridization between states in the two wells, which therefore retain a strong isolated-well character. The thickness of one period of the proposed ACQWs is between 12 and 16 nm, therefore, in order to fill the entire ridge height of a several μm thick MIR waveguide up to 500 periods are required and strain simmetrization can be achieved inserting undoped spacer layer of suitable concentration.

Optics EXPRESS

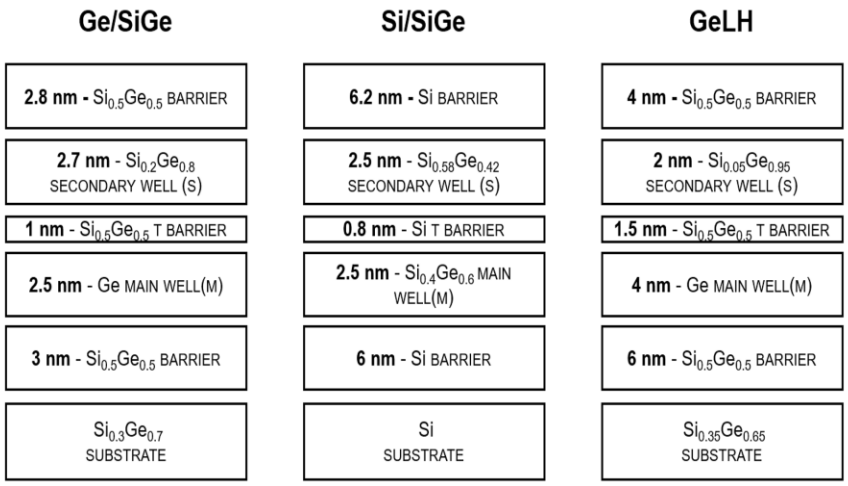

Fig. 1. Heterostructure layer scheme for the three different designs presented in this work. The epitaxial layer sequence can be identically repeated a large number of times to increase the thickness of the interaction region.

The different potential energy profiles at the valence band maximum (Γ point) for HH and LH bands are shown in Fig. 2 for the three designs. In ACQWs, the potential energy profile and the well thickness are both finely tuned in the two wells in order to engineer the energy and wavefunction symmetry of the confined electron or hole states [24–26,31]. In Fig. 2, the squared modulus of the wavefunctions of the confined states that participate to nonlinear effects for the present designs are shown as thick black curves for HH states (Fig. 2(d) and 2(e)) and as thick red lines for LH states (Fig. 2(f)). All other states are shown as thin lines with the same color code (green curves represent states in the split-off band). The ACQWs have been designed to obtain three valence subband maxima at energies E_0, E_1, E_2 with almost equal spacing $E_{01} = (E_0 - E_1) \cong (E_1 - E_2) = E_{12}$, which is a requirement for SHG [17]. The second harmonic emission takes place around $E_{02} = (E_0 - E_2)$. The SHG related parameters for the three ACQWs are reported in Table 1.

Table 1. Summary of nonlinear parameters of the ACQW structures for N_{2D} = $5.0 \cdot 10^{11} cm^{-2}$.

Design	$E_0 \rightarrow E_1 \rightarrow E_2$	T	$\chi^{(2)}_{zzz}$		$\chi^{(2)}_{xzx}$	
			$\hbar\omega$ (meV)	peak (nm/V)	$\hbar\omega$ (meV)	peak (nm/V)
Ge/SiGe	HH0M→HH0S→HH1M	10K	120	137	80	8.6
		300K	119	38	69	12.2
Si/SiGe	HH0M→HH0S→HH1M	10K	129	107	96	0.6
		300K	129	35	67	1.5
GeLH	HH0M→LH0M→LH0S	10K	78	38	94	8.9
		300K	77	10	59	15.9

Optics EXPRESS

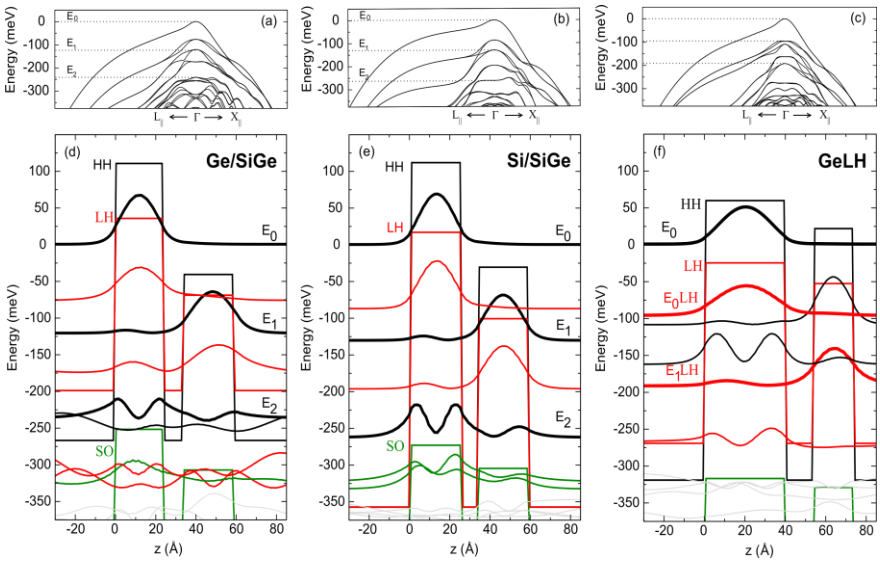

Fig. 2. (a,b,c) Valence band structure around the Γ point for the three heterostructure designs presented in this work. (d, e, f) Potential energy profile at the Γ point (straight lines) and squared modulus of the wavefunctions (curves). Heavy hole states: black, Light hole states: red, split-off band: green. The thicker curves indicate the states among which intersubband transitions responsible for the giant nonlinearity take place.

3. Calculation of nonlinear emission spectra

We have performed the novel calculations of ISBT nonlinearities for the three designs described in Fig. 1 and 2. As already pointed out for compound semiconductor materials, the p-orbital like structure of the valence band provides high values of the non-diagonal term $\chi^{(2)}_{xzx}$ of the nonlinear susceptibility tensor $\chi^{(2)}_{ijk}$. At the same time, the value of the diagonal term $\chi^{(2)}_{zzz}$ in the valence band should be of the same order (or higher) than the values calculated [33] and measured [34] for the electron-doped heterostructures materials that have been experimentally investigated up to now. Note that the indexes *i,j,k* also correspond to the required electric-field polarization directions of the output beam and of the two laser pump beams, respectively. If $j = k$, then one single laser pump beam can be used for SHG. To predict the second-order susceptibility related to ISBTs in the valence band, we rely on a semi-empirical first-neighbor $sp^3d^5s^*$ tight-binding Hamiltonian which includes spin-orbit interaction (see [32,33] for details on the model) in order to calculate the electronic band structure. In this framework, all the effects related to subband non-parabolicity and to the momentum-dependence of the dipole matrix elements, which for p-type structures are expected to play a relevant role, have been taken into account sampling the Brillouin zone around the Γ point (see Fig. 1a-c). The Brillouin zone has been sampled also along the z direction. The impact of the Hartree potential on the electronic wavefunctions is found to be negligible for all doping levels considered, therefore calculations are performed in the flat-potential approximation. In this way, we can estimate the non-linear susceptibility spectra as a function of pump photon frequency ω to obtain the SHG efficiency at 2ω from $\chi^{(2)}_{ijk}$. This is done by implementing Eq. (3).6.18) of Ref [35], where non-resonant contributions are also considered. More precisely, assuming that only the fundamental subband at E_0 is populated by holes in the zero temperature limit (Fermi level crossing the HH valence band close to the Γ point), we evaluate the third-order $\chi^{(2)}_{ijk}$ as:

Optics EXPRESS

$$\chi_{ijk}^{(2)}(2\omega) = -\int \frac{\mathrm{d}^3k}{(2\pi)^3\hbar^2}\sum_{lmn}\rho_{ll}^{(0)}(\mathbf{k})$$
$$\left(\frac{\mu_{ln}^{i}(\mathbf{k})\mu_{nm}^{j}(\mathbf{k})\mu_{ml}^{k}(\mathbf{k})}{[(\omega_{nl}(\mathbf{k})-2\omega)-i\gamma_{nl})][(\omega_{ml}(\mathbf{k})-\omega)-i\gamma_{ml}]}+\right.$$
$$\frac{\mu_{ln}^{i}(\mathbf{k})\mu_{nm}^{k}(\mathbf{k})\mu_{ml}^{j}(\mathbf{k})}{[(\omega_{nl}(\mathbf{k})-2\omega)-i\gamma_{nl})][(\omega_{ml}(\mathbf{k})-\omega)-i\gamma_{ml}]}+$$
$$\frac{\mu_{ln}^{k}(\mathbf{k})\mu_{nm}^{i}(\mathbf{k})\mu_{ml}^{j}(\mathbf{k})}{[(\omega_{mn}(\mathbf{k})-2\omega)-i\gamma_{mn})][(\omega_{nl}(\mathbf{k})+\omega)+i\gamma_{nl}]}+$$
$$\frac{\mu_{ln}^{j}(\mathbf{k})\mu_{nm}^{i}(\mathbf{k})\mu_{ml}^{k}(\mathbf{k})}{[(\omega_{mn}(\mathbf{k})-2\omega)-i\gamma_{mn})][(\omega_{nl}(\mathbf{k})+\omega)+i\gamma_{nl}]}+$$
$$\frac{\mu_{ln}^{j}(\mathbf{k})\mu_{nm}^{i}(\mathbf{k})\mu_{ml}^{k}(\mathbf{k})}{[(\omega_{nm}(\mathbf{k})+2\omega)+i\gamma_{nm})][(\omega_{ml}(\mathbf{k})-\omega)-i\gamma_{ml}]}+$$
$$\frac{\mu_{ln}^{k}(\mathbf{k})\mu_{nm}^{i}(\mathbf{k})\mu_{ml}^{j}(\mathbf{k})}{[(\omega_{nm}(\mathbf{k})+2\omega)+i\gamma_{nm})][(\omega_{ml}(\mathbf{k})-\omega)-i\gamma_{ml}]}+$$
$$\frac{\mu_{ln}^{k}(\mathbf{k})\mu_{nm}^{j}(\mathbf{k})\mu_{ml}^{i}(\mathbf{k})}{[(\omega_{ml}(\mathbf{k})+2\omega)+i\gamma_{ml})][(\omega_{nl}(\mathbf{k})+\omega)+i\gamma_{nl}]}+$$
$$\left.\frac{\mu_{ln}^{j}(\mathbf{k})\mu_{nm}^{k}(\mathbf{k})\mu_{ml}^{i}(\mathbf{k})}{[(\omega_{ml}(\mathbf{k})+2\omega)+i\gamma_{ml})][(\omega_{nl}(\mathbf{k})+\omega)+i\gamma_{nl}]}\right) \qquad (1)$$

In the above expression the index l runs over the two non-degenerate states of the fundamental subband whose energy is $E_l(\boldsymbol{k})$ while the m and n indices label the higher energy valence states; $\rho_{ll}^{(0)}(\mathbf{k})$ is the equilibrium hole distribution function of the level l and $\hbar\omega_{lm}(\boldsymbol{k}) = E_l(\boldsymbol{k}) - E_m(\boldsymbol{k})$; γ_{lm} is related to the relaxation rate for the out-of-equilibrium density matrix element ρ_{nm} and in our calculations we use a constant value, setting $\hbar\gamma = 5$ meV, in agreement with the HWHM of ISBTs typically measured in SiGe QWs systems [31,34]. Finally, dipole electric moments $\boldsymbol{\mu}_{lm} = -e\boldsymbol{r}_{lm}$ are calculated within the semi-empirical tight-binding approach following the procedure outlined in [32]. In general, a resonant peak is obtained in $\chi_{ijk}^{(2)}$ whenever one of the denominators of Eq. (1) almost vanishes, and the corresponding numerator is nonvanishing. As it can be deduced from Eq. (1), a broadening of the optical transition linewidth if compared to the discrete-level case (due to e.g. proximity of the upper state to the top of the barrier, extreme nonparabolicity of the bands, …) may results in the weakening of nonlinear response.In Fig. 3, the resulting $\chi_{zzz}^{(2)}$ spectrum is shown for the Ge/SiGe design at 10 K and at 300 K, for different values of N_{2D}. The peak position is quite stable against temperature. In Fig. 3a, the susceptibility spectrum features a dominant peak at 120 meV related to the HH0M→HH0S→HH1M transitions. The maximum calculated values of the the nonlinear coefficient are $2\cdot10^4$ pm/V for the chosen value γ = 5 meV, a value that compares well with recent reports in InGaAs/AlGaAs systems [18] and is more than two orders of magnitude higher than that of the best MIR nonlinear crystals. A weaker peak is seen at 167 meV with significant nonlinear susceptibility value due to the resonance of the HH0M→LH0S transitions with the transitions from LH0S to LH1S, LH1M and SO0M states (see Fig. 1(d)). The latter transitions involve LH states and therefore also give a nondiagonal susceptibility component $\chi_{xzx}^{(2)}$ (not shown in Fig. 3), with significant peak value $\chi_{xzx}^{(2)} = 8\cdot10^3$ pm/V at T = 10 K, and $\chi_{xzx}^{(2)} = 3.3\cdot10^3$ pm/V at T = 300 K and for $N_{2D} = 1.25\cdot10^{12}$ cm^{-2}. Notice that these numerical values strongly depend on the selected of the homogenous broadening γ

Optics EXPRESS

= 5 meV, and therefore they have to be verified by experiments, in which the actual broadening may be different.

In Fig. 3, the increase of T distributes the holes into states at finite $\boldsymbol{k}$ around the Γ point, where nonparabolicity plays a role hence making the spectral peak of $\chi^{(2)}_{ijk}$ broader than it is at low *T*. This reduces the peak value by a factor 3 for $\chi^{(2)}_{zzz}$. In the insets, it is shown that the nonlinear coefficient increases proportionally to N_{2D} up to $1{\cdot}10^{12}$ cm^{-2}, well within the achievable range of present epitaxial material growth technology. Only at T = 10 K and for $N_{2D} = 1.25{\cdot}10^{12}$ cm^{-2} the nonlinear coefficients show a trend towards saturation, again due to nonparabolicity effects arising for the filling of hole states at $\boldsymbol{k} \neq 0$.

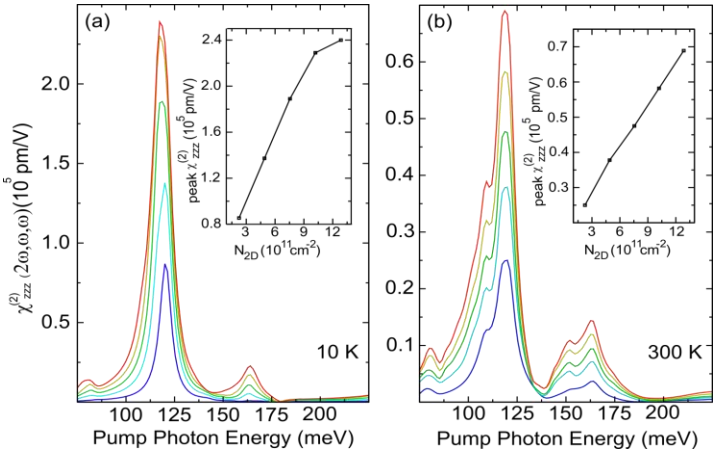

Fig. 3. Diagonal term of the modulus of the susceptibility sensor $\chi^{(2)}_{zzz}$ for the Ge/SiGe design at 10 K (a) and at 300 K (b), calculated for different free hole density levels N_{2D}: blue, $2{\cdot}10^{11}$ cm^{-2} (blue); $5{\cdot}10^{11}$ cm^{-2} (cyan); $8{\cdot}10^{11}$ cm^{-2} (green); $1.1{\cdot}10^{12}$ cm^{-2} (gold); $1.3{\cdot}10^{12}$ cm^{-2} (red). In the inset, the peak value of the susceptibility $\chi^{(2)}_{zzz}$ vs. N_{2D}.

In Fig. 4, both the $\chi^{(2)}_{zzz}$ and $\chi^{(2)}_{xzx}$ nonlinear coefficient spectra at 10 K and at 300 K are reported for all three heterostructure designs. The main numerical values (peak energy and nonlinear susceptibility value) are summarized in Table 1. According to [24], the dipole orientation of the ISBTs involving both HH and LH states, associated with energy resonance $E_{01} \cong E_{12}$, leads to peaks in $\chi^{(2)}_{xzx}$, while ISBTs involving only HH states give peaks in the $\chi^{(2)}_{zzz}$ spectrum. The Ge/SiGe design features both a high $\chi^{(2)}_{zzz}$ for laser pump frequency ω ~120 meV due to the HH0M→HH0S→HH1M transitions and a high $\chi^{(2)}_{xzx}$ for ω ~80 meV, due to the HH0M→LH0M→LH0S transitions, in addition to the peak at 167 meV, not shown in Fig. 4 but shown in Fig. 3 instead. The Si/SiGe design features only one main peak in $\chi^{(2)}_{zzz}$ at ω ~125 meV since the HH0M→LH0M→LH0S is not energy-resonant. The GeLH design at T = 10 K shows, among other minor peaks, a dominant peak at ω ~94 meV associated to the energy resonance of the HH0M→LH0M→LH0S transitions. At room *T*, due to the distribution of holes into states with $\boldsymbol{k} \neq 0$, the spectral features become more difficult to interpret in terms of a simple three-level system because of the more complicated band structure of the GeLH design depicted in Fig. 1(c). Nevertheless, the $\chi^{(2)}_{xzx}$ peak value value slightly increases with *T* although it is clearly redshifted far from the design value of 94 meV obtained at T = 10 K. In general, designs with higher $\chi^{(2)}_{zzz}$ are expected to perform better in sensor configurations including metasurfaces and nanoantenna arrays, while designs with higher $\chi^{(2)}_{xzx}$ will require two cross-polarized, counter-propagating pump beams in a waveguide, but they could lead to the relevant feature of surface emission [24], which could be of high importance in novel MIR sensor architectures (see Section 5 below).

Optics EXPRESS

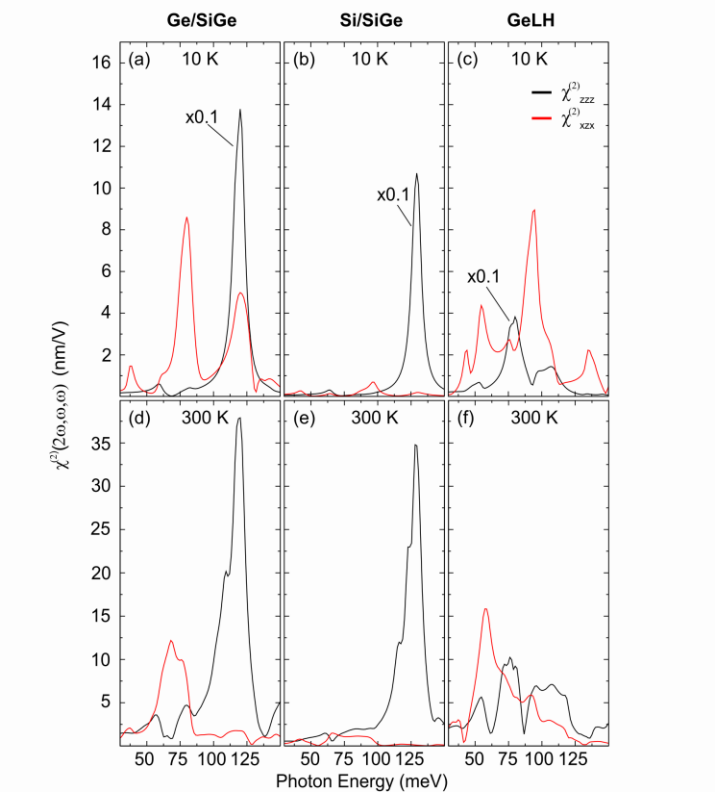

Fig. 4. Nonlinear susceptibility spectra for the three designs design at T = 10 K (a-c) and at T = 300 K (d-f) and for diagonal (black) and off-diagonal (red) tensor elements. The value of N_{2D} = $5 \cdot 10^{11}$ cm^{-2} has been considered.

4. Material growth issues

The epitaxial growth of Ge/SiGe and Si/SiGe heterostructures has undergone an impressive development in the last decade driven by the envisioned applications in the silicon photonic technology [28,30,36–39]. Nevertheless, the realization of Ge/SiGe and Si/SiGe quantum wells with narrow wells, abrupt interfaces and high compositional mismatch between the well and the barrier remains challenging. Unlike III-V semiconductors, Si and Ge are completely miscible over the entire compositional range and, therefore, the realization of atomically sharp interfaces is hindered by the natural tendency of the two elements to mix up. The intermixing between Si and Ge is mediated by native point defects, namely vacancies and interstitials, as in many other semiconductors, but the picture is further complicated by the influence of strain and composition on the diffusion mechanisms. In order to estimate the robustness of the proposed designs against the intermixing, we have repeated the calculation of the potential profile and of the wavefunctions for the Ge/SiGe design in presence of intermixing, which has been modelled for each well by a superposition of two error functions:

$$x = x_b + \frac{1}{2}(x_b - x_w)\left(erf\left(\frac{\frac{a}{2}+x}{\sqrt{2}\sigma}\right) + erf\left(\frac{\frac{a}{2}-x}{\sqrt{2}\sigma}\right)\right) \quad (2)$$

where x_B and x_W are the Ge fraction in the barrier and in the well respectively, a is the width of the ideal box-like quantum well, and σ is the standard deviation of the intermixing density.

Optics EXPRESS

The length of the intermixed region (i.e. the distance over which the composition varies from $\cong$ 90% of x_B to $\cong$ 90% of x_W) can be conventionally defined as $l = 3.3\sigma$. The quantum state calculation results are reported in Fig. 5, together with those related to the ideal case. The calculations have been performed by taking into account a realistic intermixing region length l = 1.65 nm. The energy and the squared wavefunction of the HH states are shown in Fig. 5. Clearly, the potential barriers do still exist and minor changes to the quantum states are visible with respect to the ideal case. Experimental analysis will be required in the future to calculate design corrections due to intermixing effects. Also, the effect of intermixing and alloy scattering on coherence time of the electronic states is not considered here, and it may have a major impact on line broadening hence on the intensity of nonlinear effects.

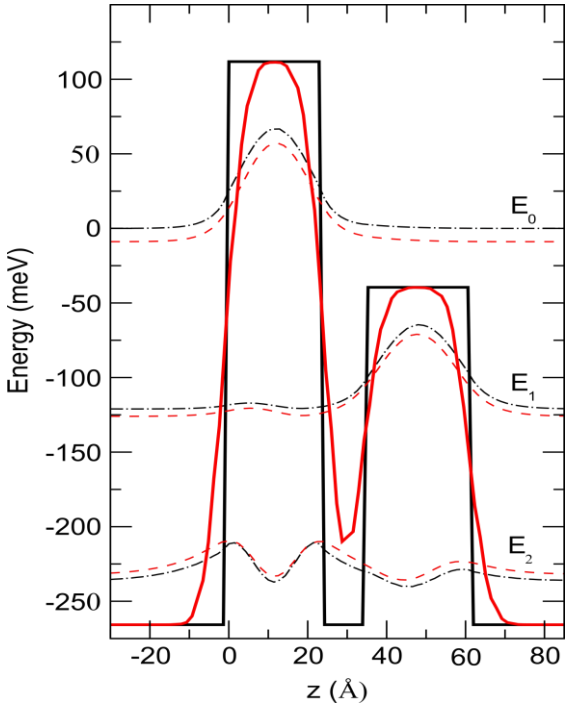

Fig. 5. Effect of the intermixing on the potential profile (ideal in black solid line, with intermixing in red solid line) and on the wavefunctions (ideal in black dash-dot line, with intermixing in red dashed line) for the Ge/SiGe design.

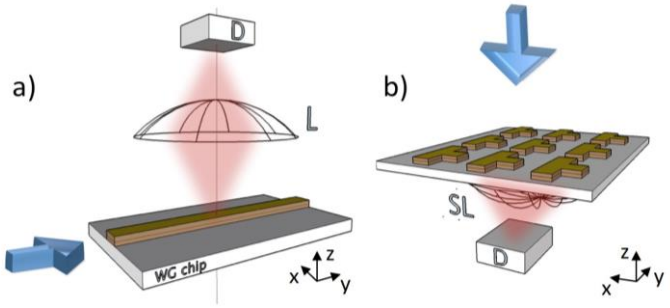

Fig. 6. Sketch of two possible sensing configurations. (a) integrated waveguides; (b) plasmonic metasurfaces. The blue arrow indicates the incoming direction of the laser pump beam, while the red shaded areas represent the propagation volumes of the emitted SHG. D: detector, L: lens, SL: substrate lens.

Optics EXPRESS

5. Perspectives and conclusions

There are two main practical configurations that have been employed to generate SHG in the MIR: laterally-pumped waveguide chips [21,25,26] and, more recently, vertically-pumped metasurfaces [17,18]. Both these configurations can be further engineered towards the realization of a MIR sensor employing Ge-Si heterostructure chips to be fabricated in silicon photonics foundries by lithography and dry etching. The silicon substrate chips could be disposable or replaceable, and they could be inserted in an optical sensing system including a pump laser in the long-wavelength infrared (LWIR, $\lambda > 8$ μm) and a MIR detector with an integrated short wavelength-pass filter.

Traditionally, waveguides have been employed to observe nonlinear effects because they guarantee long interaction regions, intrinsic spatial overlap between pump and output beams and, in the case of single-mode waveguides, also a sizeable electric field enhancement factor if compared to plane waves. The giant nonlinear response of MQWs and the strong absorption coefficient of ISBTs imply that a few hundred microns of interaction length are usually sufficient to deplete the pump beam and obtain maximum conversion efficiency [19]. Recently, state-of-the art MIR waveguides have been realized in both the Ge-on-Si and the SiGe-on-Si platforms, exploiting the difference in refractive indexes between Ge (n = 4.0) and Si (n = 3.4) in the MIR [39–42]. An example of a sensing configuration is shown in Fig. 6a, where the pump beams propagate in the waveguide in a direction y parallel to the QW plane. Both TM $(\boldsymbol{E} \parallel z)$ and TE $(\boldsymbol{E} \parallel x)$ polarizations are supported by the waveguide and the $\chi^{(2)}_{xzx}$ produces a surface emitting SHG beam propagating along z with $\boldsymbol{E} \parallel x$. Phase matching issues need to be thoroughly considered. The sensing volume is the space above the waveguide, which is probed by the vertically-emitted SHG radiation before it travels to the detector, with the target material absorbing radiation at frequency 2ω resonating with its vibrational mode in the MIR.

Nonlinear metasurfaces consisting of two-dimensional arrays of plasmonic nanoresonators, each of them containing the MQW layers in its sub-wavelength sized field-enhancement regions, have also been considered [17,18,27]. Using vertical illumination, the interaction length corresponds to the thickness of the MQW layers and therefore it is extremely short. However, the strong field enhancement provided by the resonators can be exploited to recover the high nonlinear efficiency, while also releasing selection rules and phase-matching constraints. A silicon substrate lens (see Fig. 6b) is likely to be the most suitable configuration to optimize SHG power collection. If the target material has a vibrational fingerprint either at the fundamental frequency or at the second harmonic, it will result in a measurable perturbation of the SHG process (typically, increase of losses and decrease of SHG efficiency).

In conclusion, we have explored the giant nonlinearity effect in silicon-based hole-doped $Si_{1-x}Ge_x$ heterostructures whose growth process, if compared to more common III-V semiconductor heterostructures, features cost-effective silicon foundry compatibility. Exploiting a well established tight-binding approach, we were able to take into account precisely the strong nonparabolicity of the different valence subband dispersion and the orbital symmetry of the states involved in the intersubband transitions. The first design of nonlinear frequency generation on silicon-based quantum wells are presented, and in particular we have described three different designs of asymmetric coupled quantum wells for second harmonic generation. Their practical realization and the robustness of the predicted electronic structure against intermixing effects, unavoidable in $Si_{1-x}Ge_x$, has been critically discussed. $\chi^{(2)}_{zzz}$ values in the mid-infrared range (pump photon energy between 50 meV and 170 meV) are found to be comparable to those predicted and measured in III-V quantum wells, i.e. three orders of magnitude higher than the best nonlinear crystals. Furthermore, owing to the interaction of the different valence bands (mostly heavy and light hole bands

Optics EXPRESS

with different orbital symmetry), significant values of the nondiagonal term of the susceptibility tensor $\chi^{(2)}_{xzx}$ is predicted hence enabling surface-normal second-harmonic emission, which is instead prevented in electron-doped quantum well systems. These results pave the way for nonlinear light-generation devices based on silicon wafers emitting in the mid-infrared range [43], to be used for applications such as sensors exploiting both propagation in integrated germanium-rich waveguides and surface-normal emission geometries.

Funding

Sapienza Università di Roma program "Bandi di Ateneo per la Ricerca 2017".

References

1. J. Haas and B. Mizaikoff, "Advances in Mid-Infrared Spectroscopy for Chemical Analysis," Annu. Rev. Anal. Chem. (Palo Alto, Calif.) **9**(1), 45–68 (2016).
2. R. Adato and H. Altug, "In-situ ultra-sensitive infrared absorption spectroscopy of biomolecule interactions in real time with plasmonic nanoantennas," Nat. Commun. **4**(1), 2154–2163 (2013).
3. O. Limaj, F. D'Apuzzo, A. Di Gaspare, V. Giliberti, F. Domenici, S. Sennato, F. Bordi, S. Lupi, and M. Ortolani, "Mid-Infrared Surface Plasmon Polariton Sensors Resonant with the Vibrational Modes of Phospholipid Layers," J. Phys. Chem. C **117**(37), 19119–19126 (2013).
4. Y.-C. Chang, P. Wägli, V. Paeder, A. Homsy, L. Hvozdara, P. van der Wal, J. Di Francesco, N. F. de Rooij, and H. Peter Herzig, "Cocaine detection by a mid-infrared waveguide integrated with a microfluidic chip," Lab Chip **12**(17), 3020–3023 (2012).
5. P. T. Lin, S. W. Kwok, H. Y. G. Lin, V. Singh, L. C. Kimerling, G. M. Whitesides, and A. Agarwal, "Mid-Infrared Spectrometer Using Opto-Nanofluidic Slot-Waveguide for Label-Free On-Chip Chemical Sensing," Nano Lett. **14**(1), 231–238 (2014).
6. I. Galli, S. Bartalini, S. Borri, P. Cancio, D. Mazzotti, P. De Natale, and G. Giusfredi, "Molecular gas sensing below parts per trillion: radiocarbon-dioxide optical detection," Phys. Rev. Lett. **107**(27), 270802 (2011).
7. O. Limaj, S. Lupi, F. Mattioli, R. Leoni, and M. Ortolani, "Midinfrared surface plasmon sensor based on a substrateless metal mesh," Appl. Phys. Lett. **98**(9), 091902 (2011).
8. B. G. Lee, M. A. Belkin, R. Audet, J. MacArthur, L. Diehl, C. Pflügl, F. Capasso, D. C. Oakley, D. Chapman, A. Napoleone, D. Bour, S. Corzine, G. Höfler, and J. Faist, "Widely tunable single-mode quantum cascade laser source for mid-infrared spectroscopy," Appl. Phys. Lett. **91**(23), 231101 (2007).
9. F. Neubrech, C. Huck, K. Weber, A. Pucci, and H. Giessen, "Surface-Enhanced Infrared Spectroscopy Using Resonant Nanoantennas," Chem. Rev. **117**(7), 5110–5145 (2017).
10. L. Baldassarre, E. Sakat, J. Frigerio, A. Samarelli, K. Gallacher, E. Calandrini, G. Isella, D. J. Paul, M. Ortolani, and P. Biagioni, "Midinfrared plasmon-enhanced spectroscopy with germanium antennas on silicon substrates," Nano Lett. **15**(11), 7225–7231 (2015).
11. V. Giannini, Y. Francescato, H. Amrania, C. C. Phillips, and S. A. Maier, "Fano Resonances in Nanoscale Plasmonic Systems: A Parameter-Free Modeling Approach," Nano Lett. **11**(7), 2835–2840 (2011).
12. F. B. Barho, F. Gonzalez-Posada, M. J. Milla-Rodrigo, M. Bomers, L. Cerutti, and T. Taliercio, "All-semiconductor plasmonic gratings for biosensing applications in the mid-infrared spectral range," Opt. Express **24**(14), 16175–16190 (2016).
13. M. J. Milla, F. Barho, F. González-Posada, L. Cerutti, B. Charlot, M. Bomers, F. Neubrech, E. Tournie, and T. Taliercio, "Surface-enhanced infrared absorption with Si-doped InAsSb/GaSb nano-antennas," Opt. Express **25**(22), 26651–26661 (2017).
14. T. Neuman, C. Huck, J. Vogt, F. Neubrech, R. Hillenbrand, J. Aizpurua, and A. Pucci, "Importance of Plasmonic Scattering for an Optimal Enhancement of Vibrational Absorption in SEIRA with Linear Metallic Antennas," J. Phys. Chem. C **119**(47), 26652–26662 (2015).
15. M. Celebrano, X. Wu, M. Baselli, S. Großmann, P. Biagioni, A. Locatelli, C. De Angelis, G. Cerullo, R. Osellame, B. Hecht, L. Duò, F. Ciccacci, and M. Finazzi, "Mode matching in multiresonant plasmonic nanoantennas for enhanced second harmonic generation," Nat. Nanotechnol. **10**(5), 412–417 (2015).
16. N. Leindecker, A. Marandi, R. L. Byer, K. L. Vodopyanov, J. Jiang, I. Hartl, M. Fermann, and P. G. Schunemann, "Octave-spanning ultrafast OPO with 2.6-6.1 μm instantaneous bandwidth pumped by femtosecond Tm-fiber laser," Opt. Express **20**(7), 7046–7053 (2012).
17. J. Lee, M. Tymchenko, C. Argyropoulos, P. Y. Chen, F. Lu, F. Demmerle, G. Boehm, M. C. Amann, A. Alù, and M. A. Belkin, "Giant nonlinear response from plasmonic metasurfaces coupled to intersubband transitions," Nature **511**(7507), 65–69 (2014).
18. J. Lee, N. Nookala, J. S. Gomez-Diaz, M. Tymchenko, F. Demmerle, G. Boehm, M. C. Amann, A. Alù, and M. A. Belkin, "Ultrathin Second-Harmonic Metasurfaces with Record-High Nonlinear Optical Response," Adv. Opt. Mater. **4**(5), 664–670 (2016).

Optics EXPRESS

19. C. Gmachl, A. Belyanin, D. L. Sivco, M. L. Peabody, N. Owschimikow, A. M. Sergent, F. Capasso, and A. Y. Cho, "Optimized second-harmonic generation in quantum cascade lasers," IEEE J. Quantum Electron. **39**(11), 1345–1355 (2003).
20. R. Soref, "Mid-infrared photonics in silicon and germanium," Nat. Photonics **4**(8), 495–497 (2010).
21. L. Zhang, A. M. Agarwal, L. C. Kimerling, and J. Michel, "Nonlinear Group IV photonics based on silicon and germanium: from near-infrared to mid-infrared," Nanophotonics **3**(4-5), 247–268 (2014).
22. M. P. Fischer, C. Schmidt, E. Sakat, J. Stock, A. Samarelli, J. Frigerio, M. Ortolani, D. J. Paul, G. Isella, A. Leitenstorfer, P. Biagioni, and D. Brida, "Optical activation of germanium plasmonic antennas in the mid-infrared," Phys. Rev. Lett. **117**(4), 047401 (2016).
23. I. Razdolski, Y. Chen, A. J. Giles, S. Gewinner, W. Schöllkopf, M. Hong, M. Wolf, V. Giannini, J. D. Caldwell, S. A. Maier, and A. Paarmann, "Resonant Enhancement of Second-Harmonic Generation in the Mid-Infrared Using Localized Surface Phonon Polaritons in Subdiffractional Nanostructures," Nano Lett. **16**(11), 6954–6959 (2016).
24. S. Li and J. Khurgin, "Second-order nonlinear optical susceptibility in p-doped asymmetric quantum wells," Appl. Phys. Lett. **62**(15), 1727–1729 (1993).
25. E. Rosencher, A. Fiore, B. Vinter, V. Berger, Ph. Bois, and J. Nagle, "Quantum Engineering of Optical Nonlinearities," Science **271**(5246), 168–173 (1996).
26. K. L. Vodopyanov, K. O'Neill, G. B. Serapiglia, C. C. Phillips, M. Hopkinson, I. Vurgaftman, and J. R. Meyer, "Phase-matched second harmonic generation in asymmetric double quantum wells," Appl. Phys. Lett. **72**(21), 2654–2656 (1998).
27. O. Wolf, S. Campione, A. Benz, A. P. Ravikumar, S. Liu, T. S. Luk, E. A. Kadlec, E. A. Shaner, J. F. Klem, M. B. Sinclair, and I. Brener, "Phased-array sources based on nonlinear metamaterial nanocavities," Nat. Commun. **6**(1), 7667 (2015).
28. Y. H. Kuo, Y. K. Lee, Y. Ge, S. Ren, J. E. Roth, T. I. Kamins, D. A. B. Miller, and J. S. Harris, "Strong quantum-confined Stark effect in germanium quantum-well structures on silicon," Nature **437**(7063), 1334–1336 (2005).
29. H. Durmaz, P. Sookchoo, X. Cui, R. B. Jacobson, D. E. Savage, M. G. Lagally, and R. Paiella, "SiGe Nanomembrane Quantum-Well Infrared Photodetectors," ACS Photonics **3**(10), 1978–1985 (2016).
30. P. Chaisakul, D. Marris-Morini, J. Frigerio, D. Chrastina, M. S. Rouifed, S. Cecchi, P. Crozat, G. Isella, and L. Vivien, "Integrated germanium optical interconnects on silicon substrates," Nat. Photonics **8**(6), 482–488 (2014).
31. D. Sabbagh, J. Schmidt, S. Winnerl, M. Helm, L. Di Gaspare, M. De Seta, M. Virgilio, and M. Ortolani, "Electron Dynamics in Silicon–Germanium Terahertz Quantum Fountain Structures," ACS Photonics **3**(3), 403–414 (2016).
32. M. Virgilio and G. Grosso, "Valence and conduction intersubband transitions in SiGe, Ge-rich, quantum wells on [001] $Si_{0.5}Ge_{0.5}$ substrates: A tight-binding approach," J. Appl. Phys. **100**(9), 093506 (2007).
33. M. Virgilio and G. Grosso, "Valley splitting and optical intersubband transitions at parallel and normal incidence in [001]-Ge/SiGe quantum wells," Phys. Rev. B Condens. Matter Mater. Phys. **79**(16), 165310 (2009).
34. M. De Seta, G. Capellini, Y. Busby, F. Evangelisti, M. Ortolani, M. Virgilio, G. Grosso, G. Pizzi, A. Nucara, and S. Lupi, "Conduction band intersubband transitions in Ge/SiGe quantum wells," Appl. Phys. Lett. **95**(5), 051918 (2009).
35. R. W. Boyd, *Nonlinear Optics* (Academic Press, 2002, ISBN: 9780121216825).
36. P. Chaisakul, D. Marris-Morini, M.-S. Rouifed, J. Frigerio, D. Chrastina, J.-R. Coudevylle, X. L. Roux, S. Edmond, G. Isella, and L. Vivien, "Recent progress in GeSi electro-absorption modulators," Sci. Technol. Adv. Mater. **15**(1), 014601 (2013).
37. L. Lever, Z. Ikonic, A. Valavanis, J. Cooper, and R. Kelsall, "Design of Ge-SiGe Quantum-Confined Stark Effect Electroabsorption Heterostructures for CMOS Compatible Photonics," J. Lit. Technol. **28**, 3273–3281 (2010).
38. K. Gallacher, P. Velha, D. J. Paul, S. Cecchi, J. Frigerio, D. Chrastina, and G. Isella, "1.55 μm direct bandgap electroluminescence from strained n-Ge quantum wells grown on Si substrates," Appl. Phys. Lett. **101**(21), 211101 (2012).
39. M. Brun, P. Labeye, G. Grand, J.-M. Hartmann, F. Boulila, M. Carras, and S. Nicoletti, "Low loss SiGe graded index waveguides for mid-IR applications," Opt. Express **22**(1), 508–518 (2014).
40. A. Malik, M. Muneeb, Y. Shimura, J. Van Campenhout, R. Loo, and G. Roelkens, "Germanium-on-silicon mid infrared waveguides and Mach Zehnder interferometers," in *Proceedings of IEEE Conference on Photonics* (IEEE IPC, 2013), pp. 104–105.
41. J. M. Ramirez, V. Vakarin, C. Gilles, J. Frigerio, A. Ballabio, P. Chaisakul, X. L. Roux, C. Alonso-Ramos, G. Maisons, L. Vivien, M. Carras, G. Isella, and D. Marris-Morini, "Low-loss Ge-rich $Si_{0.2}Ge_{0.8}$ waveguides for mid-infrared photonics," Opt. Lett. **42**(1), 105–108 (2017).
42. J. M. Ramirez, Q. Liu, V. Vakarin, J. Frigerio, A. Ballabio, X. Le Roux, D. Bouville, L. Vivien, G. Isella, and D. Marris-Morini, "Graded SiGe waveguides with broadband low-loss propagation in the mid infrared," Opt. Express **26**(2), 870–877 (2018).
43. D. J. Paul, "The progress towards terahertz quantum cascade lasers on silicon substrates," Laser Photonics Rev. **4**(5), 610–632 (2010).